Properties of the Satellite Photoelectron Sheath Derived from Photoemission Laboratory Measurements

RÉJEAN J. L. GRARD

*Space Science Department, European Space Research and Technology Centre
Noordwijk, The Netherlands*

The electrical properties of the medium around a probe in the outer magnetosphere and in interplanetary space are modified by photoemission. Information on the energy distribution of the photoemitted electrons is important for the evaluation of the physical parameters of the surrounding photosheath and for the interpretation of the probe measurements. This energy distribution has been determined for various materials exposed to sunlight, at the earth's orbit, by combining laboratory measurements on photoemission with solar spectrum data collected in space. It is found that the photoelectron saturation current density is a function of the material and can vary from a few microamperes per square meter up to several tens of microamperes per square meter; the photoelectron density is of the order of 10^2–10^3/cm^3 in the vicinity of the probe. The shape of the distribution is approximately Maxwellian, and the mean kinetic energy is of the order of 1.5 ev. Current voltage characteristics and conductance of surfaces emitting photoelectrons are also derived. A number of photosheath parameters, such as shielding distance and surface electric field, are tabulated. Finally, the consequences of photoemission for the interpretation of space measurements are discussed.

The plasma density is reduced to a few particles per cubic centimeter beyond a distance of 3–4 R_E. There the electrical properties in the environment of a body, such as a satellite, the moon, or an interstellar grain, are strongly affected by emission of photoelectrons from its surface. The importance of this problem is acknowledged by most experimenters interested in measurements beyond the plasmapause.

Theoretical considerations [*Grard and Tunaley*, 1971] and computer simulations [*Grard*, 1970; *Soop*, 1972] have already improved our understanding of this phenomenon, but it has been found desirable to complement this work by surface physics experiments in the laboratory [*Feuerbacher and Fitton*, 1972]. The purpose of this study is to combine solar spectrum data collected in space [*Allen*, 1955; *Friedman*, 1963; *Hinteregger et al.*, 1965] and photoemission measurements made in the laboratory, to predict the electric properties of various materials irradiated by sunlight. An accurate knowledge of this energy distribution is essential for predicting, for example, the extent of the photoelectron cloud around a spacecraft, the value of the electric impedance of probes, the strength

of electric drag on interstellar grain, or the magnitude of the electric field on the lunar surface.

This study is based on laboratory measurements made by *Feuerbacher and Fitton* [1972], who discussed in detail the solid state aspect of this phenomenon. The materials, which have been selected in their experimental study, are those which are used in space technology, such as aluminum, stainless steel, and gold, or those which could be used as conductive coating on solar cells array, such as indium oxide. Lithium fluoride has also been included, because it is possible to control photoemission by coating a surface with a layer of this material. Finally, various carbon compounds, such as graphite, Aquadag (produced by Acheson Colloids N.V., Schiedam, Holland), and vitreous carbon (produced by Vitreous Carbon Ltd., Bishop Auckland, England), have also been chosen, because the uniformity of their work function is an interesting property for dc electric field and Langmuir probe experiments [*Trendelenburg et al.*, 1970].

In this paper we compute the energy distribution of photoelectrons emitted from these materials in sunlight; we derive the current voltage characteristic and the ac electric con-

ductance of probes made of these materials. Other parameters of the photosheath are also given, such as the electron density and electric field on the surface. The effect of the ambient plasma is also discussed, and typical values are given for the floating potential of the surface. A similar study dealing with the lunar surface has been presented elsewhere [*Feuerbacher et al.*, 1972].

For clarification, a list of symbols is given in appendix 2.

EXPERIMENTAL RESULTS

Data on the Solar Flux

The knowledge of the solar photon energy distribution at the earth's orbit is essential for the study of photoemission in space. Measurements of the energy spectrum $S(w)$ per sec m² ev are shown in Figure 1 against the photon energy w in electron volts. These data have been collected by *Allen* [1955], *Friedman* [1963] and *Hinteregger et al.* [1965] and have been gathered by *Walbridge* [1971].

The continuous component of the solar spectrum is approximated by a histogram, and its magnitude decreases by nearly 6 orders of magnitude between 4 and 12 ev. The accuracy
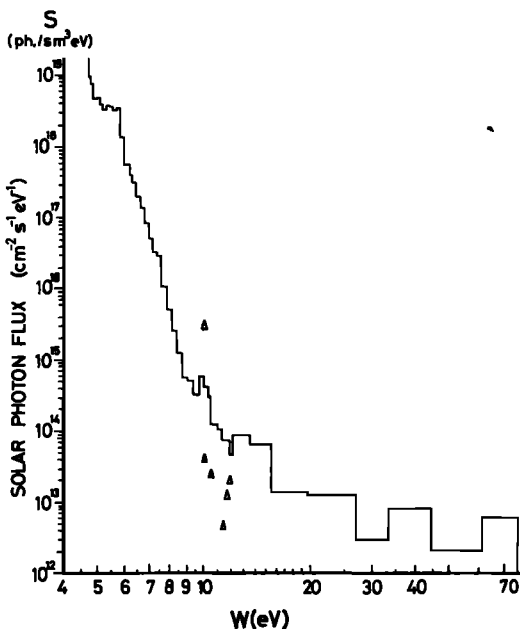
and resolution of the measurements are good in the lower energy range but are much less satisfactory above 15 ev.

A number of discrete lines exists superimposed on this continuous spectrum. Each line can be conveniently included in the spectrum in the form of a Dirac pulse, which is generally represented by a spike, the height of which is indicated by a triangle in Figure 1. The flux corresponding to a line is equal to the area under the corresponding pulse, which is obtained by multiplying the height of the spike by 1 ev. It is easily seen, for example, that the flux associated with the Lyman α line, which is the most important line of the solar spectrum, is of the order 2.7×10^{15} photons per sec m².

Laboratory Measurements

Photoelectron yield. The photoelectric yield $Y(w)$, i.e., the number of emitted electrons per incoming photon for a given photon energy w, has been measured in the laboratory for a number of selected materials. The results, which are displayed in Figures 2a–9a, have been obtained by *Feuerbacher and Fitton* [1972] under near normal light incidence; more details on the experimental conditions can be found in their paper.

The abscissa of the point where the axes intersect is the work function w_f of the sample, the values of which are listed in Table 2 and lie between 4 and 5 ev for most of the materials under consideration. The maximum yield is reached at approximately 10 ev above the work function; this maximum value does not exceed 3% for graphite (Figure 9a) but attains 30% for indium oxide and lithium fluoride (Figures 3a and 7a, respectively).

Fig. 1. The solar flux energy spectrum measured in space.

Fig. 2. (Opposite) Experimental results, aluminum oxide. (*a*) Photoelectric yield per incoming photon versus photon energy. (*b*) Differential photoelectron flux versus photon energy under perpendicular solar irradiation. (*c*) Normalized photoelectron energy distribution curves for different incident photon energies. (*d*) Normalized photoelectron energy distribution curves under solar irradiation (left-hand scale) or per-unit-area conductances (right-hand scale) versus probe potential, associated with a planar probe (full line) or a small sample (dashed line). (*e*) Normalized photoelectron fluxes (left-hand scale) or current densities (right-hand scale) versus probe potential, corresponding to a planar probe (full line) or a small sample (dashed line).
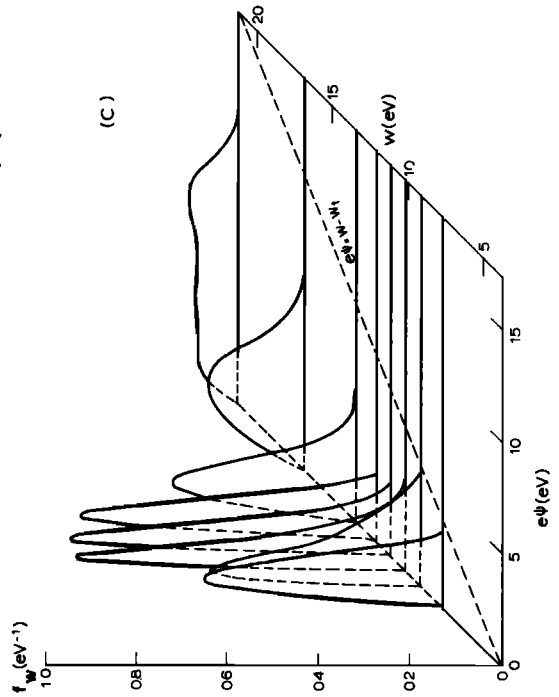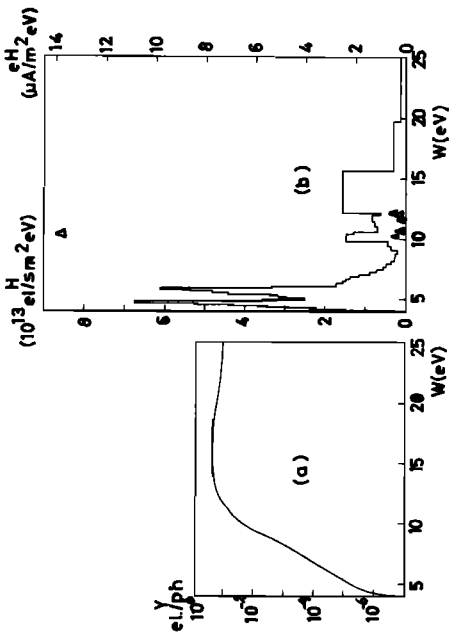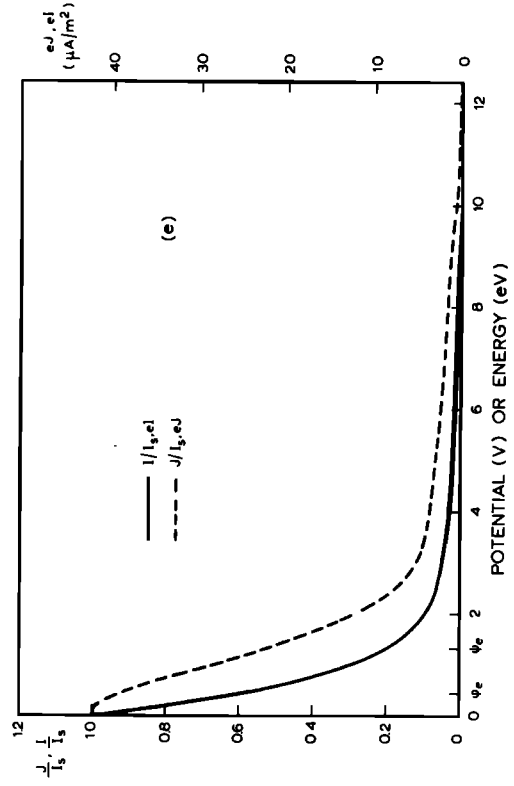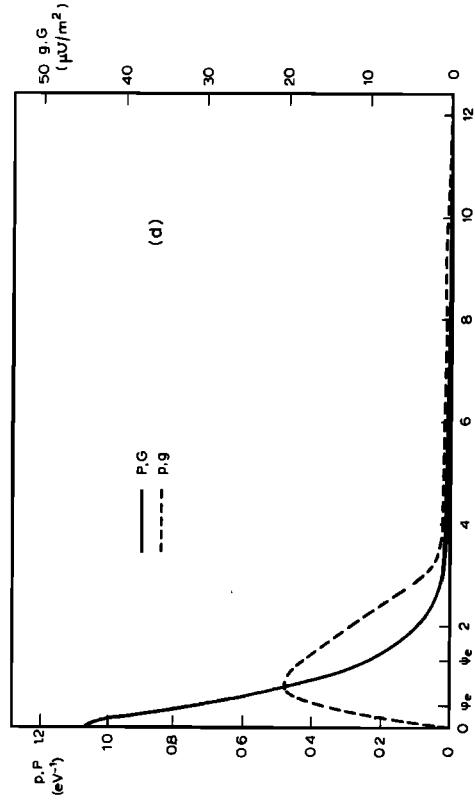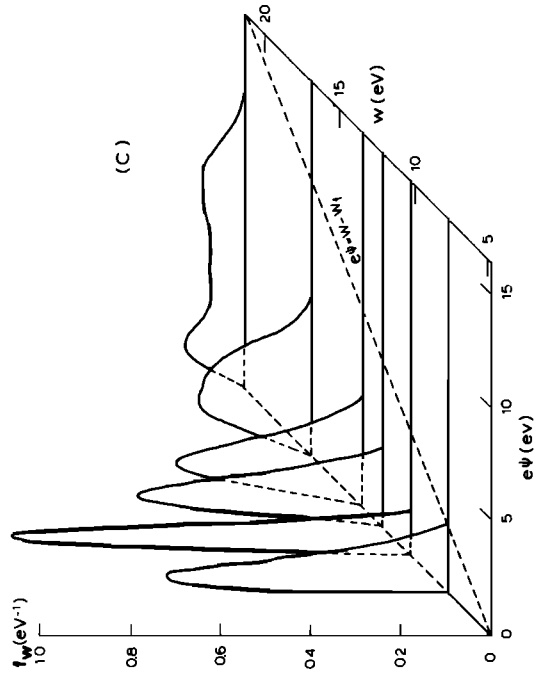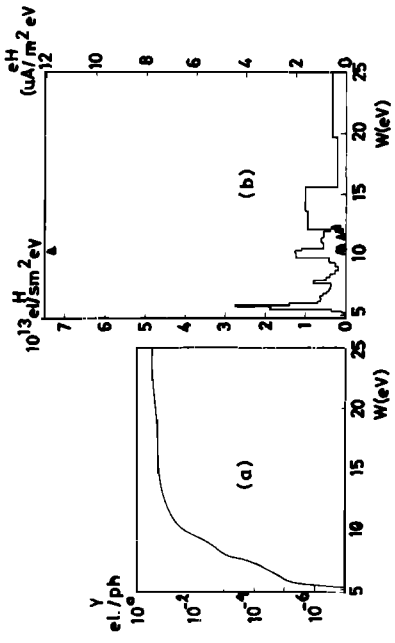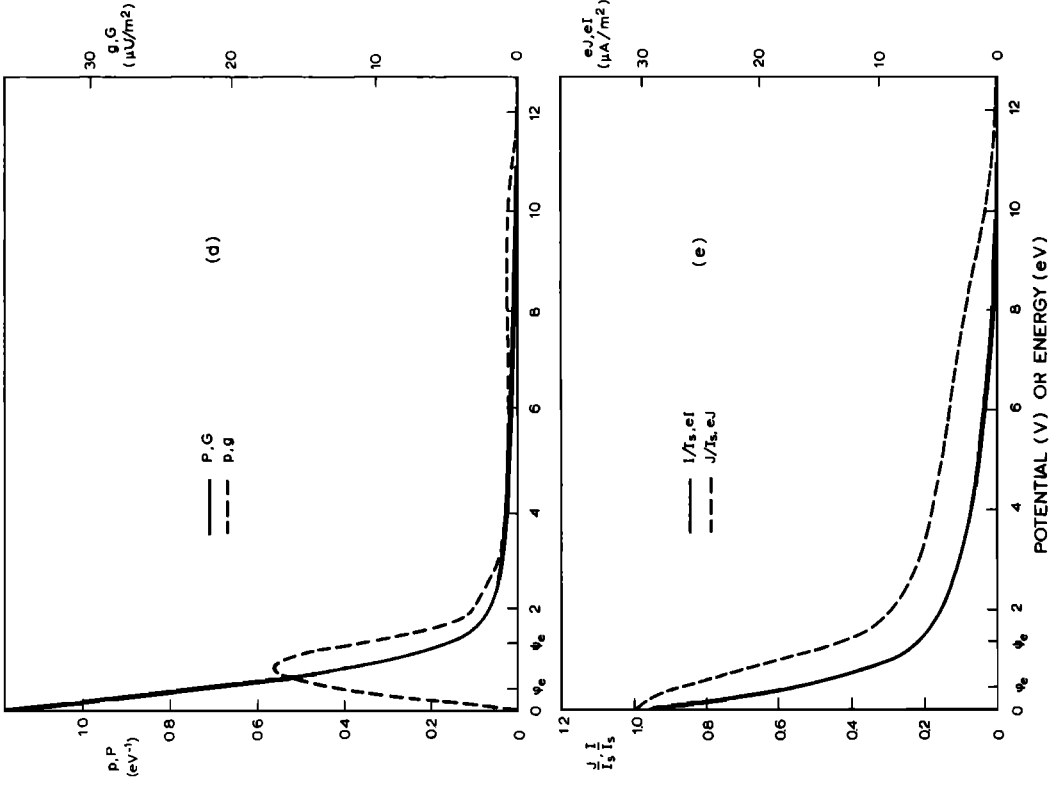
Owing to experimental limitations, no yield measurements were made for photon energies above 21 ev. However, for the purpose of this study, the yield for aluminum was extrapolated at higher energies in a way such as to drop to 10^{-3} at 120 ev, as measured by *Lukirskii et al.* [1960]. For other materials this model was scaled by a factor proportional to the yield measured at 21 ev.

Multiplying the differential yield by the solar flux energy spectrum, we obtain the differential flux of photoelectrons emitted under solar irradiation,

$$H(w) = S(w) Y(w) \qquad (1)$$

which is measured in photoelectrons per sec m² ev; the results are shown in Figures 2b–9b. The vertical scale has been kept the same on all figures to allow comparisons between different materials; the photon energy is measured along a horizontal axis similar to that of parts *a* of the figures. The contributions due to solar lines are indicated by triangles, the most important being, for all materials, that of the Lyman α line. This differential flux is a function of the photon energy w, and should not be confused with the photoelectron energy distribution.

Integrating (1) with respect to w, we obtain the total flux of photoelectrons per sec m² emitted by a material irradiated by sunlight under normal incidence:

$$I_s = \int_0^\infty H(w) \ dw \qquad (2)$$

Values of I_s for different materials are listed in Table 2. Multiplying the electron flux by the elementary charge yields the saturation photocurrent density eI_s, which is also given in Table 2. It is seen, for example, that the current density is approximately 40 $\mu A/m^2$ for aluminum oxide and an order of magnitude lower for graphite.

Photoelectron energy distribution. The photoelectron energy distribution has been measured in the laboratory for various photon energies. The set of curves shown in Figures 2c–

9c represents all the data available for this study and have been made by following the results given by *Feuerbacher and Fitton* [1972] or data privately communicated by the first author. The electron energy distribution for monochromatic light $f_w(\psi)$ is plotted against the electron energy $e\psi$ for fixed values of the photon energy w. The graduation of the photon energy axis is so chosen that it corresponds to that used in parts *a* and *b* of the figures. Each energy distribution curve has been normalized in a way such that the area under it is equal to unity; i.e.,

$$\int_0^\infty f_w(\psi) d\psi = 1 \qquad (3)$$

The straight line of equation

$$e\psi = w - w_f \qquad (4)$$

has also been drawn; it indicates that the maximum energy with which an electron is emitted cannot exceed the energy of the incident photon minus the work function of the material.

The photoelectron energy distribution under solar irradiation is found by multiplying the energy spectrum for monochromatic light $f_w(\psi)$ by the differential electron flux $H(w)$ and integrating with respect to the photon energy. This is written

$$p(\psi) = \frac{1}{I_s} \int_0^\infty f_w(\psi) H(w) \ dw \qquad (5)$$

note that $p(\psi)$ is normalized in a way such that

$$\int_0^\infty p(\psi) \ d\psi = 1 \qquad (6)$$

The quantity $I_s p(\psi)$ is a differential flux, and it is correct to refer to the function $p(\psi)$ as an energy distribution, since its dimension is per electron volts. If confusion is to be avoided, it is important to note that this may be for some readers an unorthodox use of the term. Our definition of $p(\psi)$ is that the flux of particles with energies between ψ and $\psi + \Delta\psi$, not their volume density, is proportional to $p(\psi)\Delta\psi$. This convention has the practical advantage that the energy distribution is directly linked to interesting physical parameters, such as the conductance and the current voltage characteristic of a probe. The correspondence

---

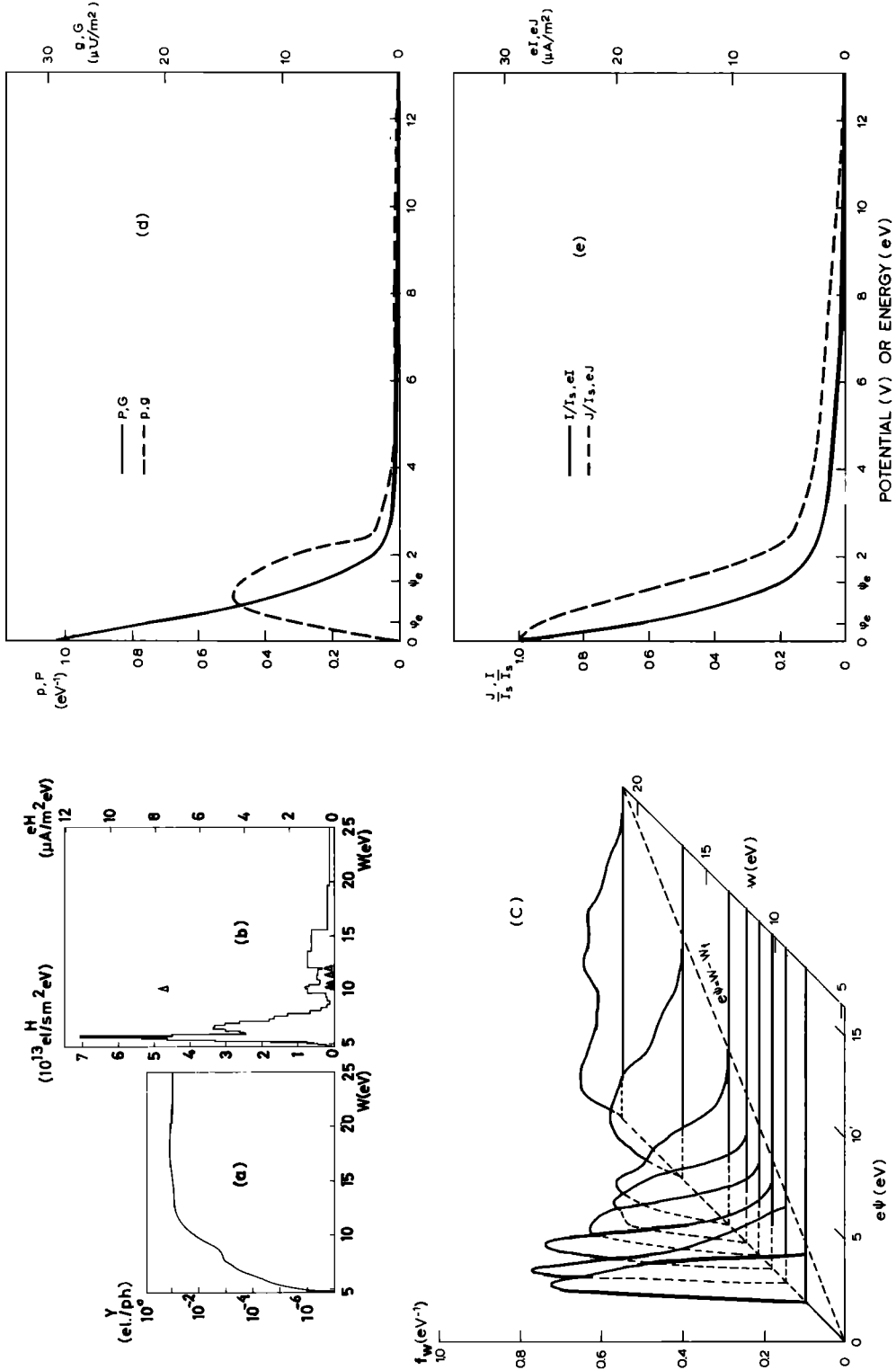Fig. 3. (Opposite) Experimental results, indium oxide coating (see the legend of Figure 2 for details).

Fig. 4. Experimental results, gold (see the legend of Figure 2 for details).

Fig. 5. Experimental results, stainless steel (see the legend of Figure 2 for details).

Fig. 6.   Experimental results, Aquadag (see the legend of Figure 2 for details).

Fig. 7. Experimental results, gold with 200-Å lithium fluoride overcoating (see the legend of Figure 2 for details).

Fig. 8.   Experimental results, vitreous carbon (see the legend of Figure 2 for details).

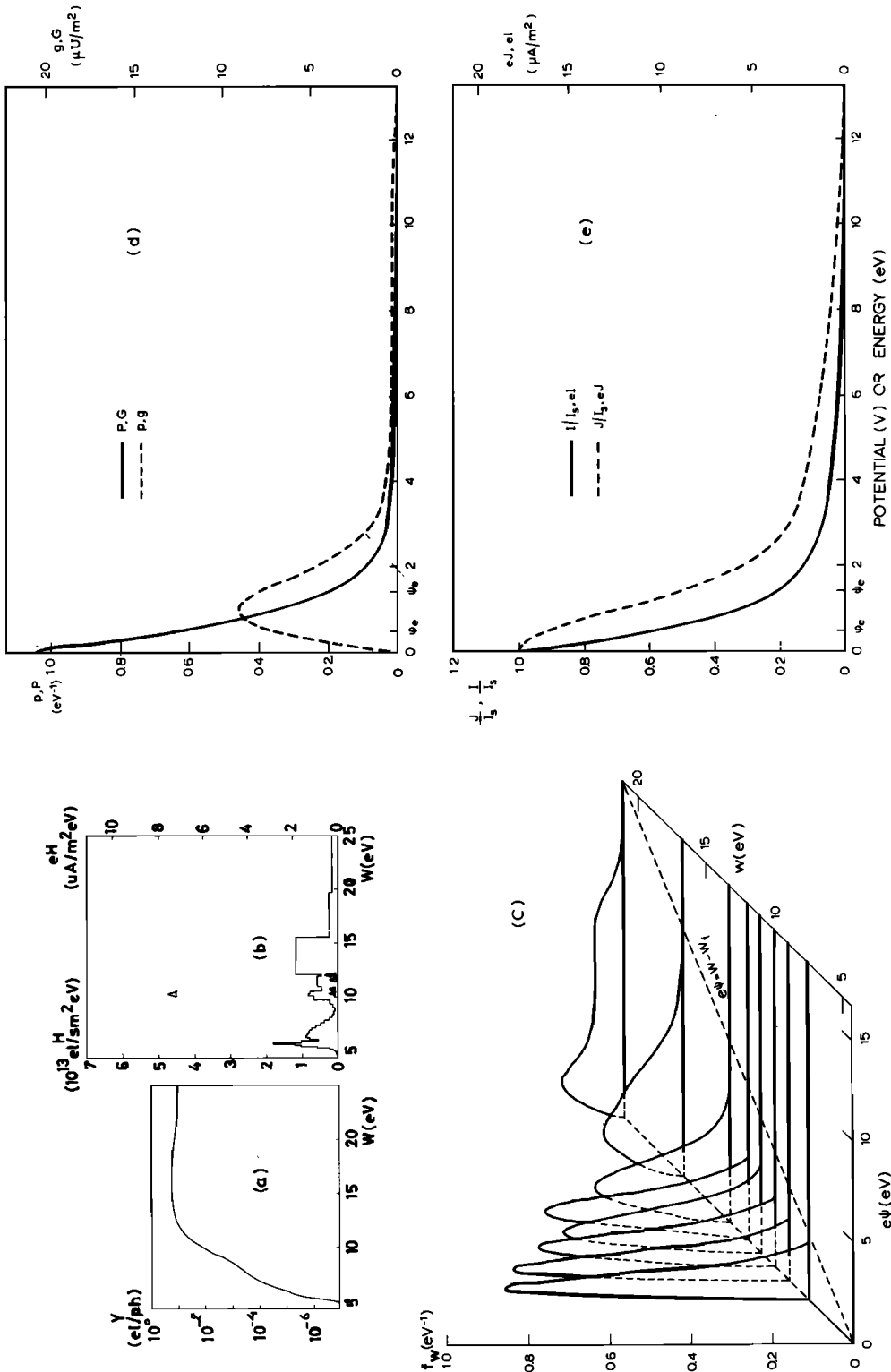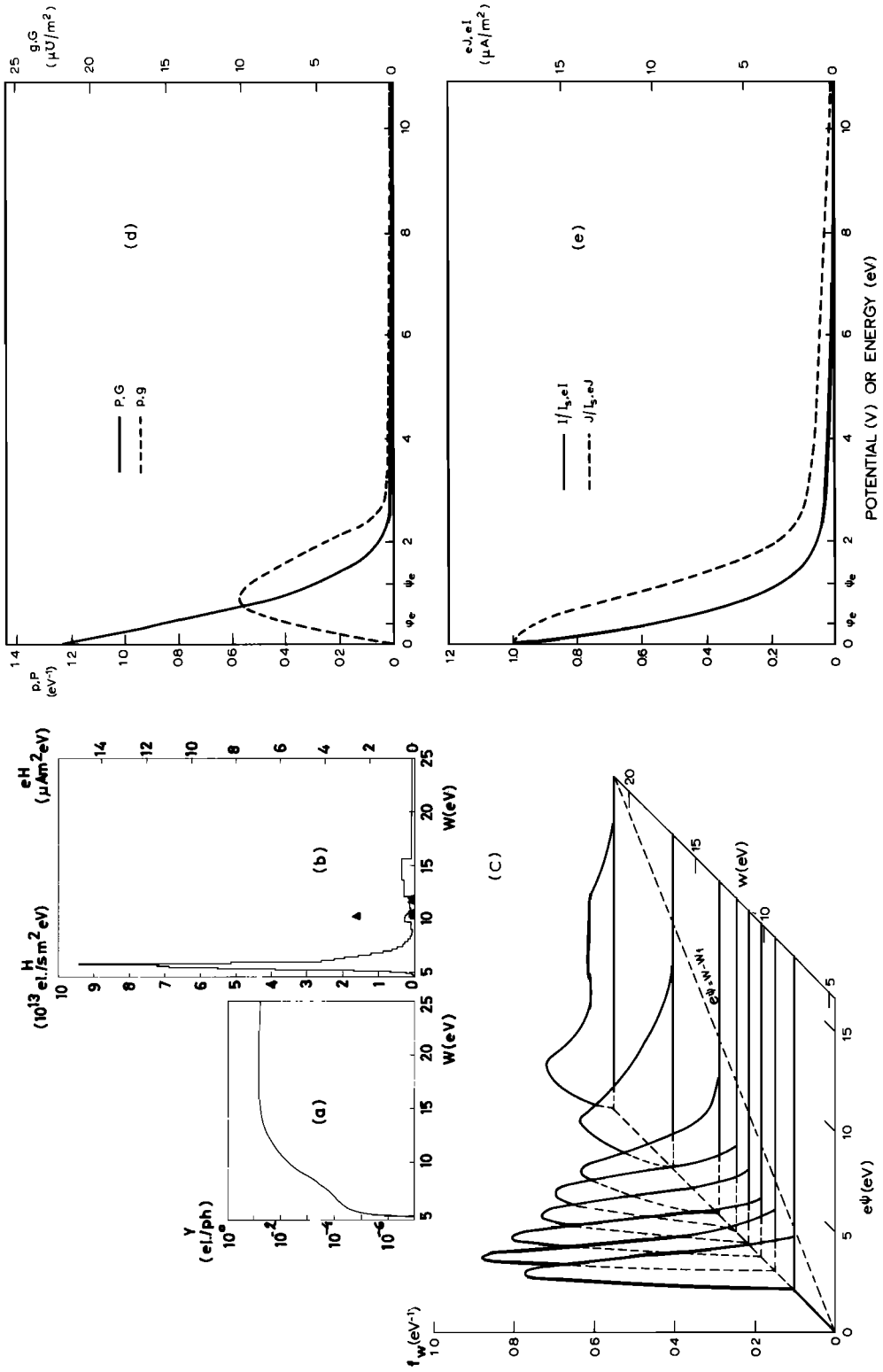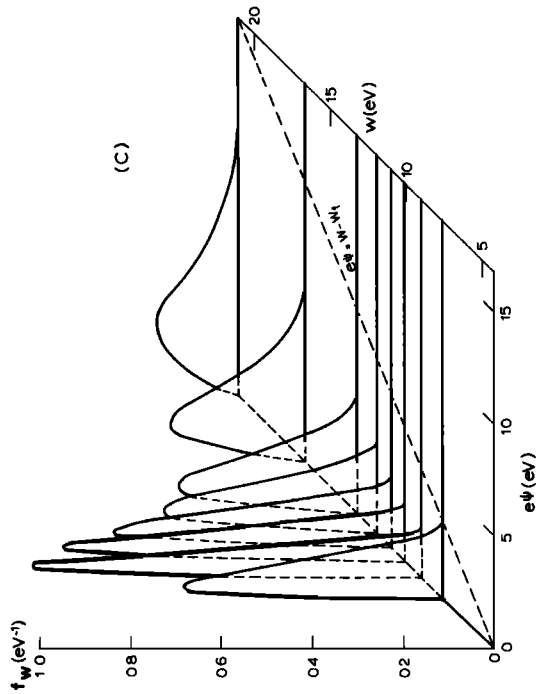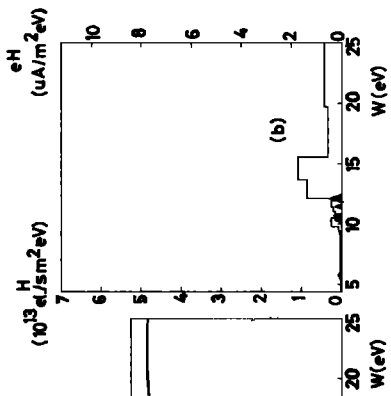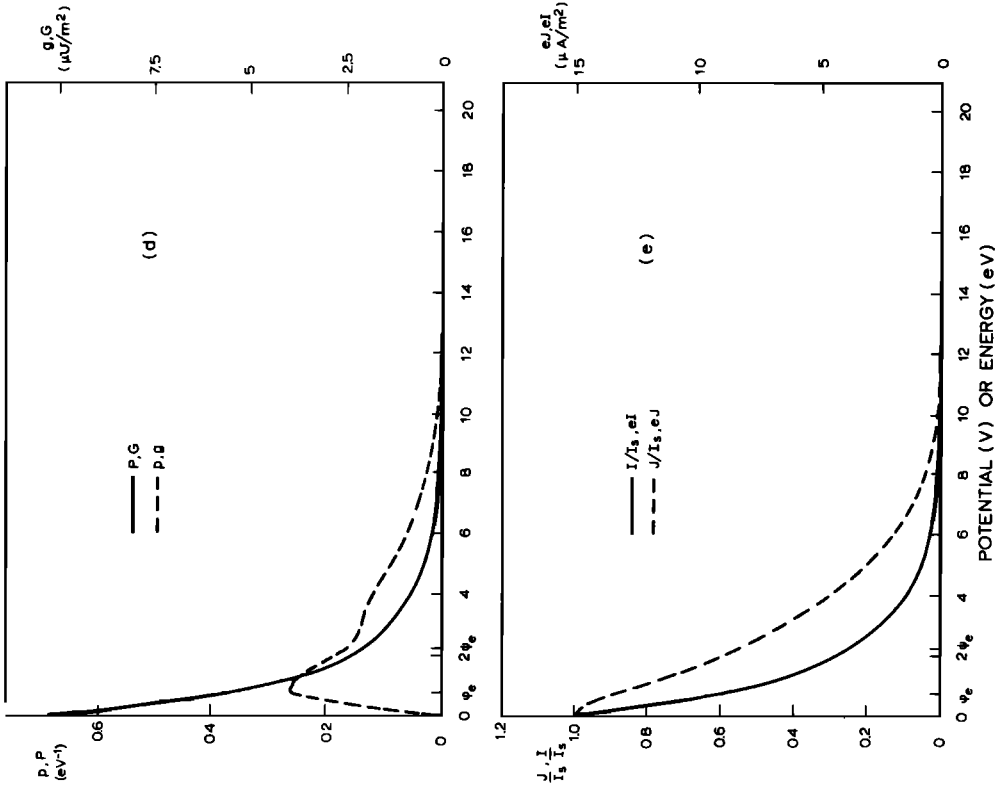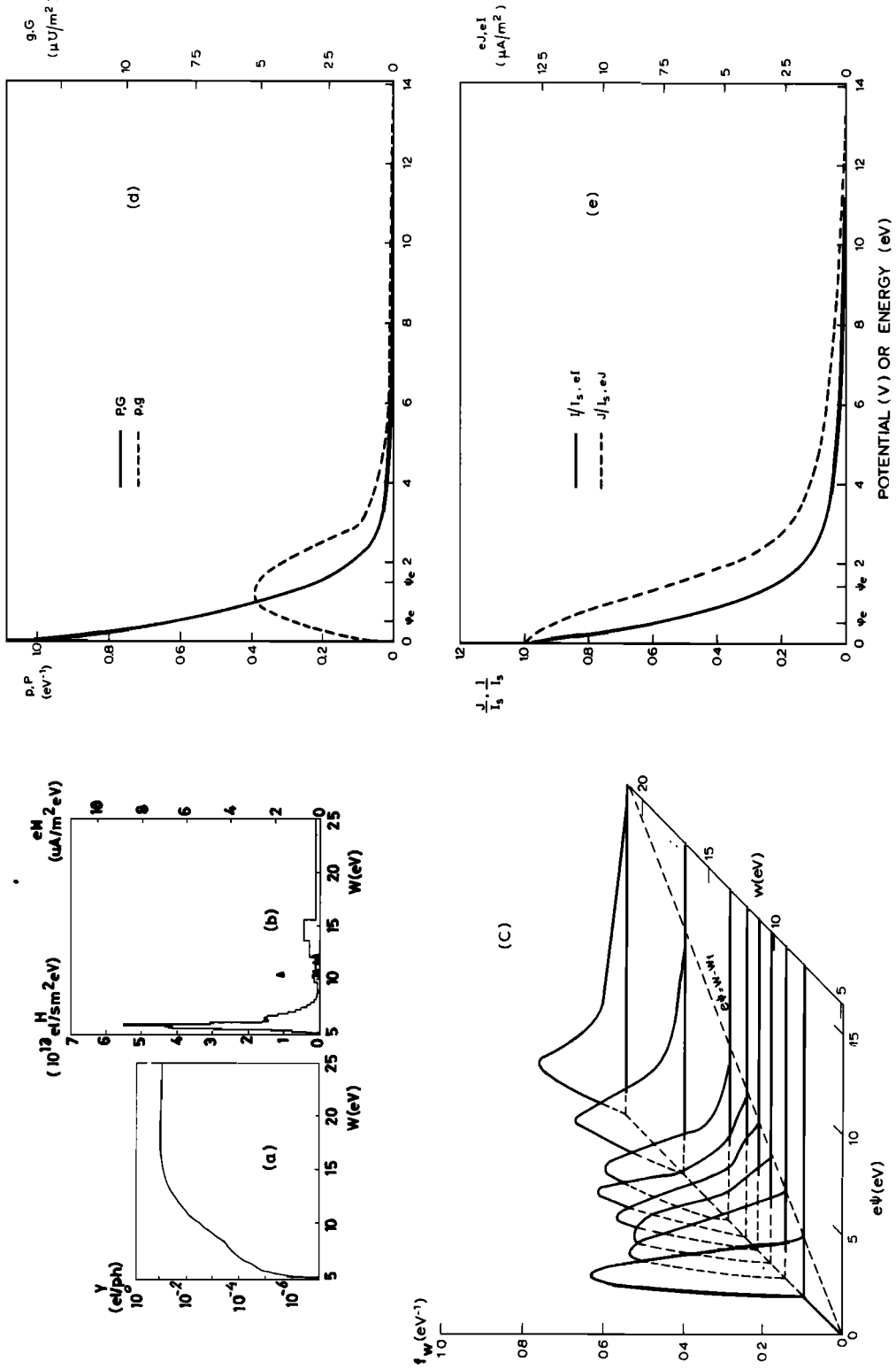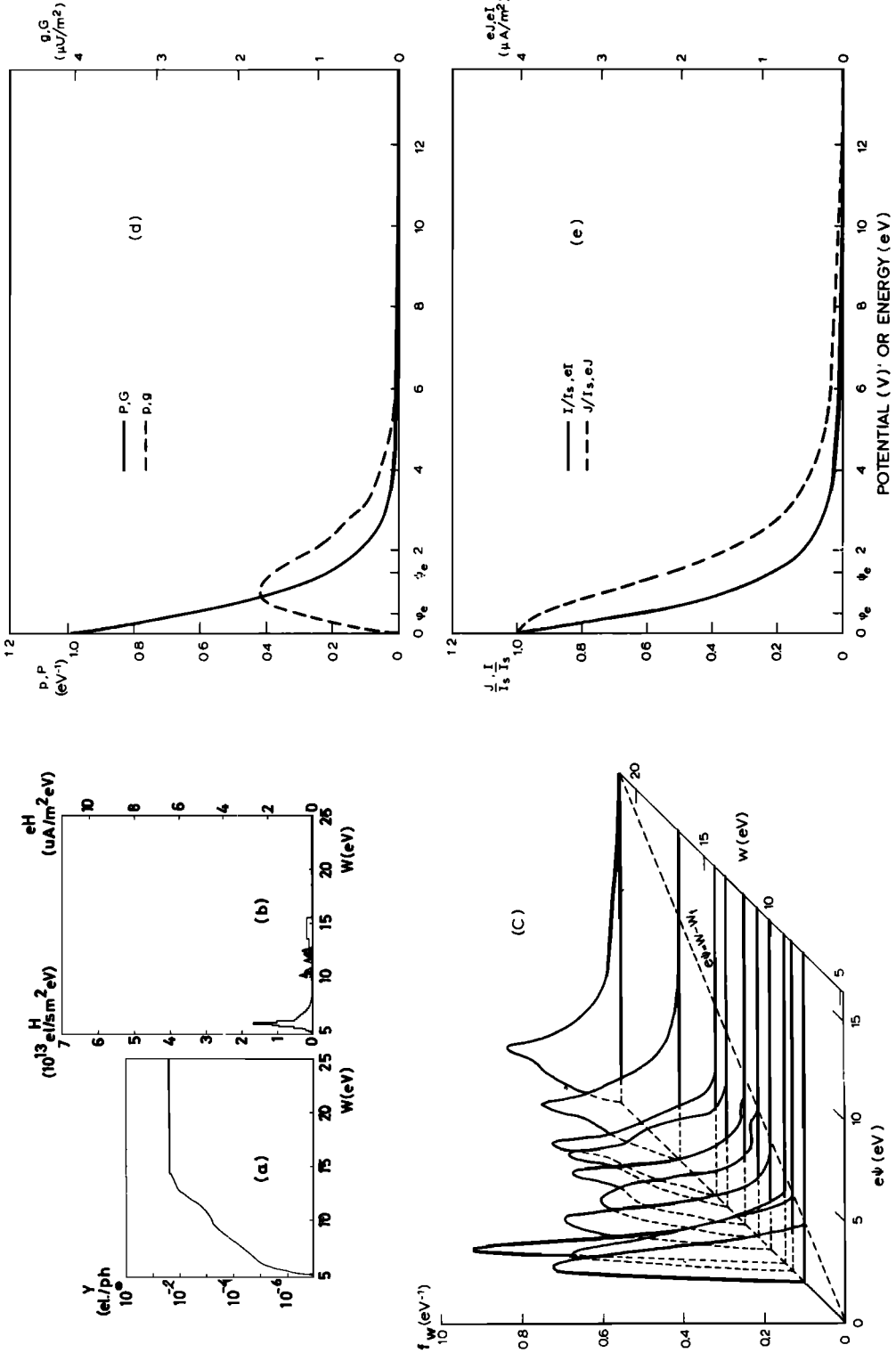Fig. 9. Experimental results, graphite (see the legend of Figure 2 for details).

TABLE 1. Recapitulation of the Theoretical Results

Distribution Function	Arbitrary	Monoenergetic	Maxwellian
Energy distribution $p(\psi)$	Measured	$\delta(\psi - \psi_0)$	$\psi/\phi_0^2 \exp(-\psi/\phi_0)$
Mean kinetic energy $e\psi_e$	$(8me)^{1/2} \dfrac{I_e}{N_0} \displaystyle\int_0^\infty (\psi)^{1/2} p(\psi)\, d\psi$	$e\psi_0$	$\tfrac{3}{2}e\phi_0$
Most probable energy $e\psi_p$	$p(\psi)$ max for $\psi = \psi_p$	$e\psi_0 = \tfrac{1}{2}mu_0^2$	$e\phi_0 = \tfrac{1}{2}mv_0^2$
Max conductance per unit area, point source g_0	$eI_e p(\psi_p)$	∞	$0.368 eI_e/\phi_0$
Speed distribution $f(u)$	$\dfrac{1}{2\pi}\left(\dfrac{m}{e}\right)^2 \dfrac{I_e}{N_0} \dfrac{p(\psi)}{\psi}$	$\dfrac{1}{4\pi u_0^2}\delta(u - u_0)$	$\dfrac{1}{\pi^{3/2}v_0^3}\exp\left(-\dfrac{u^2}{v_0^2}\right)$
Mean square speed $u_e^2 = 2e\psi_e/m$	$4\pi \displaystyle\int_0^\infty u^4 f(u)\, du$	u_0^2	$\tfrac{3}{2}v_0^2$
Point source flux $J(\psi')$	$I_e \displaystyle\int_{\psi'}^\infty p(\psi)\, d\psi$	$I_e\Pi\left(\dfrac{\psi'}{\psi_0} - \dfrac{1}{2}\right)$	$I_e\left(1 + \dfrac{\psi'}{\phi_0}\right)\exp\left(-\dfrac{\psi'}{\phi_0}\right)$
Energy distribution associated with perpendicular motion $P(\phi)$	$\displaystyle\int_\phi^\infty \dfrac{p(\psi)}{\psi}\, d\psi$	$\dfrac{1}{\psi_0}\Pi\left(\dfrac{\phi}{\psi_0} - \dfrac{1}{2}\right)$	$\dfrac{1}{\phi_0}\exp\left(-\dfrac{\phi}{\phi_0}\right)$
Energy associated with rms perpendicular velocity $e\phi_e = e\psi_e/3$	$(2me)^{1/2} \dfrac{I_e}{N_0} \displaystyle\int_0^\infty (\phi)^{1/2}P(\phi)\, d\phi$	$\tfrac{1}{3}e\psi_0$	$\tfrac{1}{2}e\phi_0$
Average energy associated with perpendicular motion $e\phi_a$	$e\displaystyle\int_0^\infty P(\phi)\phi\, d\phi$	$\tfrac{1}{2}e\psi_0$	$e\phi_0$
Max conductance per unit area, planar surface G_e	$eI_e P(0)$	eI_e/ψ_0	eI_e/ϕ_0
Perpendicular velocity distribution $F(v)$	$\dfrac{2m}{e} \dfrac{I_e}{N_0} P(\phi)$	$\dfrac{1}{u_0}\Pi\left(\dfrac{v}{u_0} - \dfrac{1}{2}\right)$	$\dfrac{2}{(\pi)^{1/2}v_0}\exp\left(-\dfrac{v^2}{v_0^2}\right)$
Mean square perpendicular velocity $v_e^2 = 2e\phi_e/m$	$\displaystyle\int_0^\infty v^2 F'(v)\, dv$	$\tfrac{1}{2}u_0^2$	$\tfrac{1}{2}v_0^2$
Planar source flux $I(\phi')$	$I_e \displaystyle\int_{\phi'}^\infty \left(1 - \dfrac{\phi}{\psi}\right)p(\psi)\, d\psi$	$I_e\left(1 - \dfrac{\phi'}{\psi_0}\right)\Pi\left(\dfrac{\phi'}{\psi_0} - \dfrac{1}{2}\right)$	$I_e \exp\left(-\dfrac{\phi'}{\phi_0}\right)$
Electron volume density /saturation flux N_0/I_e	$\left(\dfrac{8m}{e}\right)^{1/2} \displaystyle\int_0^\infty \dfrac{p(\psi)}{(\psi)^{1/2}}\, d\psi$	$\dfrac{4}{u_0}$	$\dfrac{2(\pi)^{1/2}}{v_0}$

between energy distribution and the more familiar velocity distribution is clarified in the appendices.

The photoelectron energy spectrum under solar irradiation is shown in Figures 2d–9d for different materials. The scale for the function p is marked along the left vertical axis, and the electron energy is counted along the horizontal axis in electron volts. Parameters such as the mean kinetic energy $e\psi_e$ and the most probable energy $e\psi_p$ are defined in Table 1, and their values are listed in Table 2. The most striking feature is that these energies are very similar for all materials; the mean kinetic ener-

gies lie in the range 1.2–1.5 ev, with the exception of lithium fluoride, and the most probable energies are all of the order of 1 ev.

Electric Properties of Photoemissive Surfaces

Probe geometry. In a vacuum the equilibrium potential of a body under solar irradiation is such that all photoelectrons must return to its surface after being emitted. However, if a probe is polarized at a potential less than its equilibrium potential, a part of the photocurrent is emitted. Conversely, in a space experiment a small flux of ambient electrons to the body allows an equal flux of the most energetic

TABLE 2. Recapitulation of the Experimental Results

	Aluminum Oxide	Indium Oxide	Gold	Stainless Steel	Aquadag	LiF on Au	Vitreous Carbon	Graphite	Average Model	Mono-energetic	Maxwellian Model
Work function w_f, ev	3.9	4.8	4.8	4.4	4.6	4.4	4.8	4.7	Not applicable		
Electron saturation flux I_s, 10^{12}/sec m²	260	190	180	120	110	90	80	25	130	130	130
Saturation current density, eI_s, μa/m²	42	30	29	20	18	15	13	4	21	21	21
Mean kinetic energy $e\psi_s$, ev	1.33	1.36	1.40	1.42	1.17	2.24	1.51	1.48	1.42	1.42	1.42
Most probable energy $e\psi_p$, ev	0.87	0.87	0.88	0.98	0.90	0.87	1.17	1.04	0.94	1.42	0.95
Average energy associated with perpendicular motion $e\phi_o$, ev	0.94	1.19	1.02	1.06	0.83	1.57	1.10	1.02	1.07	0.71	0.95
Maximum conductance per unit area, point source g_o, μmhos/m²	20	17	14	9	10	4	5	2	10	8	8
Maximum conductance per unit area, planar source G_o, μmhos/m²	45	35	30	21	21	10	13	4	23	15	22
Electron volume sensity near the surface N_o, 10^6/m³	1670	1260	1110	770	750	460	500	150	830	750	820
Shielding distance λ_o, meters	0.17	0.20	0.22	0.26	0.24	0.42	0.34	0.60	0.25	0.26	0.25
Electric field on the surface E_o, v/m	7.4	6.5	6.1	5.2	4.6	5.0	4.3	2.4	5.4	5.1	5.3
Sheath electron content per unit area σ_o, 10^6/m²	410	360	340	280	260	280	240	130	300	280	290

photoelectrons to escape, and the potential of the probe is related to the flux leaving the surface.

The knowledge of the current voltage characteristic of the probe is therefore essential for the determination of its equilibrium potential; in addition, the derivative of this characteristic curve yields the ac conductance of the probe at low frequencies. The contribution of the surrounding plasma to the incremental conductance of the probe can be neglected when the energy of the ambient particles is much higher than that of the photoelectrons and the incoming flux is not influenced by the probe potential.

Let us now define a shielding distance for the photoelectrons analogous to the Debye length in a plasma:

$$\lambda_0 = (\tfrac{2}{3}\epsilon_0\psi_e/N_0e)^{1/2} \qquad (7)$$

where $e\psi_e$ is the mean kinetic energy of the photoelectrons when they are emitted and N_0 is the electron volume density near the surface.

We consider two extreme situations; first the probe is assumed to be a small sample, or a point source, which means that its size is much smaller than λ_0; then we treat the case of a planar surface, the dimensions of which are much larger than λ_0. These two geometries are illustrated in Figure 10.

In first approximation the equipotential surfaces are spherical around a point source. If the photoelectrons are emitted radially out of the sample, the distance at which they are reflected is a function of their initial energy but is independent of the direction along which they have been emitted, as can be seen in Figure 10a. The situation is somewhat different for a planar surface; the equipotential surfaces are planar and the distance at which an electron is reflected is now a function of the orientation
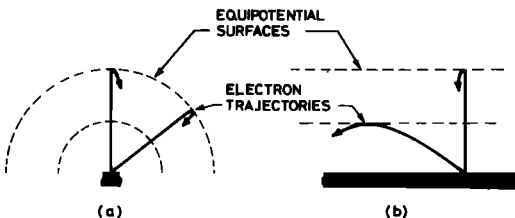
of the velocity vector with which the electron is emitted. An electron with a velocity vector perpendicular to the surface will reach a much higher distance above the surface than an electron with the same initial speed but emitted at a lower angle, as is shown in Figure 10b.

It is hoped that the results obtained under these two extreme assumptions will bracket the orders of magnitude pertaining to bodies of arbitrary size.

Small sample. If the potential of a small probe with respect to space potential is ψ', photoelectrons emitted with energies higher than $e\psi'$ do not return to the probe surface. The flux of these particles is simply related to the surface potential through the integral

$$J(\psi') = I_s \int_{\psi'}^{\infty} p(\psi) \, d\psi \qquad (8)$$

It is seen that the saturation flux is reached for $\psi' = 0$ when the probe is at space potential.

The photoelectron flux is plotted in Figures 2e–9e as a function of the probe potential; the value of the normalized flux J/I_s is indicated on the left vertical axis, whereas the corresponding current density eJ is shown on the right vertical axis in microamperes per square meter.

The low-frequency per unit area conductance of the probe $g(\psi')$ is simply given by the derivative of the current density with respect to the probe potential:

$$g(\psi') = -e \frac{dJ(\psi')}{d\psi'} = eI_sp(\psi') \qquad (9)$$

where the minus sign stands for the fact that positive currents are directed into the surface. The functions g and p are therefore represented by the same curve in parts d of the figures, but the scale for the per unit area conductance in μmhos/m^2 is shown on the right vertical axis.

The maximum conductance

$$g_0 = eI_sp(\psi_p) \qquad (10)$$

is reached when the probe potential corresponds to the most probable energy in the distribution, $e\psi_p$. Values of g_0 are listed in Table 2; they range from 2 to 20 μmhos/m^2.

Planar surface. The electric properties of a large planar probe depend on the particle motion along a direction perpendicular to its surface. Therefore the knowledge of the energy

Fig. 10. Probe geometry. (a) Small sample. (b) Planar surface.

$e\phi$ associated with the perpendicular component of the velocity is more important than that of the total electron energy $e\psi$, which has been considered so far.

The energy distribution associated with the perpendicular motion $P(\phi)$ can be derived for a given material from the total energy distribution $p(\psi)$. The detail of this treatment can be found in the appendix, and the main result is given by (A29). The only assumption to be made in this derivation is given by (A6) and concerns the angular dependence of the directional flux. Photoemission is taken to be isotropic, which is realistic for amorphous materials such as those presented in this study but would not necessarily hold for monocrystals or for finely powdered substances.

The energy distribution associated with the perpendicular motion of the electrons, $P(\phi)$, is plotted in Figures 2d–9d; the reference axes are the same as for the function $p(\psi)$.

The energy associated to the rms velocity component along the perpendicular to the plane, $e\phi_e$, is defined in Table 1. As photoemission is isotropic, this energy is equal to one third of the mean kinetic energy $e\psi_e$. The magnitudes of ϕ_e and ψ_e are shown on the horizontal axes in parts d and e of the figures.

The average energy of this distribution, $e\phi_a$, is also defined in Table 1, and its values, which are listed in Table 2, are all of the order of 1 ev.

The flux of escaping photoelectrons as a function of the surface potential ϕ' is given by

$$I(\phi') = I_s \int_{\phi'}^{\infty} P(\phi) \, d\phi \qquad (11)$$

Replacing (A29) into (11), we obtain, after some manipulation,

$$I(\phi') = I_s \int_{\phi'}^{\infty} \left(1 - \frac{\phi'}{\psi}\right) p(\psi) \, d\psi \qquad (12)$$

The saturation flux is reached when $\phi' = 0$; by comparing (8) and (12) it is checked that the saturation flux is the same for an infinite planar surface as for a small planar surface, for given material and light incidence.

The curves representing the normalized photoelectron flux I/I_s and the current density eI are displayed in Figures 2e–9e in the same manner as the corresponding curves for a small sample.

The per unit area conductance of a planar probe is given by the derivative of the current density with respect to the probe potential:

$$G(\phi') = -e\frac{dI(\phi')}{d\phi'} = eI_s P(\phi') \qquad (13)$$

The function G is represented by the same curve as P, but the corresponding scale is shown along the vertical left axis.

The maximum per unit area conductance,

$$G_0 = eI_s P(0) \qquad (14)$$

is obtained when the probe is at space potential. Values of G_0 are listed in Table 2. It is seen that for a given material the maximum per unit area conductance is about twice as much for a planar surface as for a small sample.

The electron volume density in the vicinity of the probe surface, N_0, is given by (A30). A point is said to be in the vicinity of the surface if it is at a distance much less than the shielding distance λ_0 defined by (7) in the case of a large planar probe or much less than the size of the probe in the case of a small sample.

It is implied in the theoretical treatment, which leads to (A30), that the density of the particles leaving the surface is the same as that of those returning to it; this means that the probe potential is supposed to be such that the flux of photoelectrons that is not returning to the surface, given by (8) or (12), is small as compared to the saturation flux I_s.

The values of N_0, which are recapitulated in Table 2, lie in the range 10^2–10^3 el/cm³; these electron densities are about 2 orders of magnitude larger than that of the ambient plasma beyond the plasmapause.

The shielding distance λ_0 has also been computed from (7); typical values are shown in Table 2 and are all of the order of a fraction of a meter. The shielding distance gives an order of magnitude of the sheath thickness, but the profile of the sheath is strongly influenced by the exact shape of the photoelectron energy distribution function.

The electric field on the surface of a planar probe, as well as the surface density of the positive charge carried by the probe, can be analytically derived. The electric field on the surface,

$$E_0 = 2(2)^{1/2}\psi_e/3\lambda_0 \qquad (15)$$
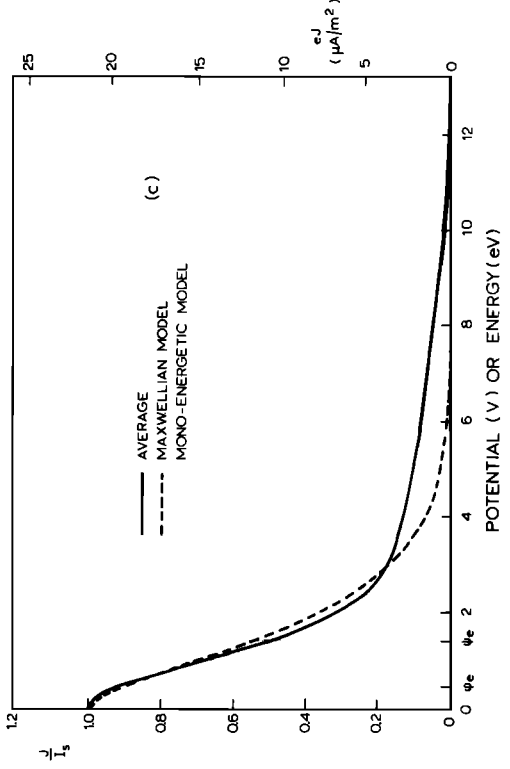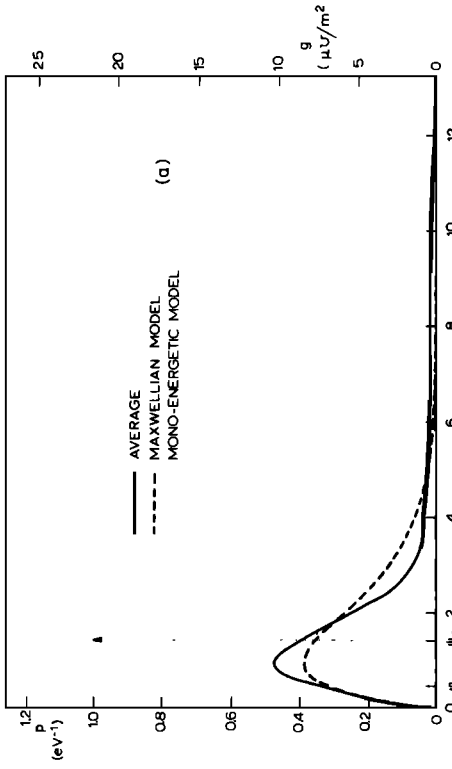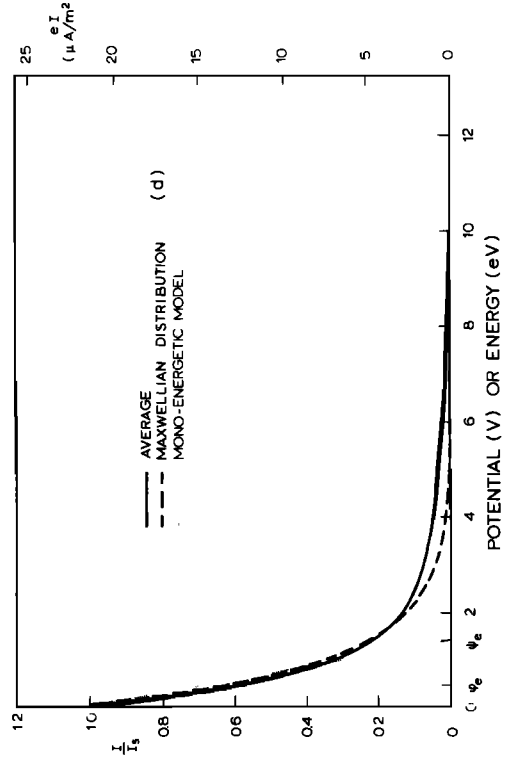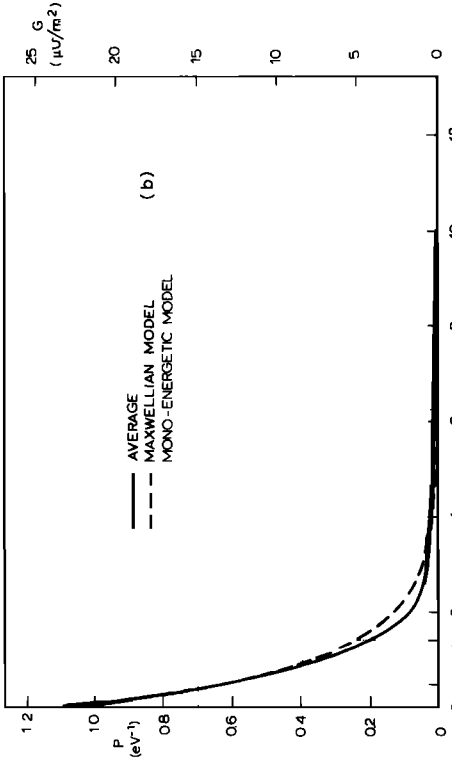
is of the order of a few volts per meter, as can be observed in Table 2. The surface density number of the positive charge carried by a planar probe,

$$\sigma_0 = (2)^{1/2} N_0 \lambda_0 \qquad (16)$$

is also equal to the columnar content of the photoelectron sheath, which is the electron volume density integrated throughout the sheath along a direction perpendicular to the surface; values of σ_0 are also given in Table 2.

DISCUSSION

Accuracy Problems

The accuracy with which the differential photoelectron flux $H(w)$ is obtainable is limited by the resolution of the solar spectrum measurements above 15 ev and by the lack of information about photoelectron yield $Y(w)$ above 21 ev. It can be checked, however, that the contribution due to photons with energies higher than 20 ev is generally not important and that the determination of the total saturation flux I_s is not very sensitive to inaccuracies in material yield and solar spectrum data for high photon energies.

The photoelectron energy distribution $f_w(\psi)$ has been measured for a limited number of photon energy values w. The shape of the distribution for an arbitrary photon energy can be safely determined by interpolation especially for values of w below 15 ev, but extrapolation is more hazardous above 20 ev. Consequently, the integrated energy distribution under solar irradiation $p(\psi)$ is satisfactorily defined for the bulk of the low-energy photoelectrons, but the accuracy corresponding to the high-energy tail, say for values of ψ above 10 ev, may be questionable. The limitations of this technique can be appreciated by comparing the figures for the saturation current of aluminum oxide given

here, 42 $\mu a/m^2$, with that directly measured in space, 30 $\mu a/m^2$ [Whipple, 1965]. This discrepancy, however, is also due to differences in cleanliness, roughness, and oxidation of the samples [Grard and Tunaley, 1971].

Models for the Energy Distribution

Each material is characterized by its yield curve $Y(w)$ and its energy distribution surface $f_w(\psi)$. However, all the normalized energy distribution curves $p(\psi)$ present similar features. It seems therefore meaningful to look for models that will represent the shape of the energy distribution for all materials.

One can, for example, consider an average model defined by

$$p(\psi) = \sum_i [I_{si} p_i(\psi)] / \sum_i I_{si}, \qquad (17)$$

where the subscript i refers to each material individually and the sums are taken over all materials considered in this study. It is found that the mean kinetic energy associated to this model is 1.42 ev and that the average saturation current density is 21 $\mu a/m^2$.

One may also attempt to approximate an experimental energy distribution using an analytical model; the simplest of all is the monoenergetic model

$$p(\psi) = \delta(\psi - \psi_0) \qquad (18)$$

where δ is the Dirac function; electrons are isotropically emitted with the same energy $e\psi_0$. Analytical results, which can be derived using this type of distribution, are given in Table 1 (it is recalled that the rectangular $y = h\Pi(x - a)$ is such that $y = h$ for $a - \frac{1}{2} < x < a + \frac{1}{2}$ and that $y = 0$ elsewhere).

The Maxwellian model is defined by

$$p(\psi) = (\psi/\phi_0^2) \exp(-\psi/\phi_0) \qquad (19)$$

where $e\phi_0$ is the most probable energy. Analytical results associated with this distribution are found in Table 1; it is seen that the current-conductance ratio for a planar probe is constant and given by

$$eI(\phi)/G(\phi) = \phi_0 \qquad (20)$$

The average monoenergetic and Maxwellian models are compared in Figure 11. The energy distributions displayed in Figure 11a have the

---

Fig. 11. (Opposite) Comparison between three energy distribution models with identical mean kinetic energies: normalized photoelectron energy distribution curves (left-hand scale) or per unit area conductances (right-hand scale) versus probe potential associated with (a) a small sample and (b) a planar probe; normalized photoelectron fluxes (left-hand scale) or current densities (right-hand scale) corresponding to (c) a small sample and (d) a planar probe.

same mean kinetic energy. The right vertical axis has been graduated in microvolts per square meter, since the same curves also represent the per unit area conductance for a small sample; it is assumed that the saturation current density is the same for the analytical models as for the average model. The corresponding curves for a planar surface are displayed in Figure 11b. In addition, the current density characteristics for a small sample and a planar surface, respectively, have been drawn for the three models in Figure 11(c, d). More numerical comparisons have been made in Table 2.

It is seen in Figure 11 that a typical experimental energy distribution, such as that obtained with the average model, can be approximated by a Maxwellian distribution. It is also shown in Table 2 that parameters that characterize the photoelectron sheath, such as N_0, λ_0, E_0, and σ_0, are practically not affected by the shape of the energy distribution.

Effect of a Tenuous Ambient Plasma

In the absence of ambient plasma the photocurrent emitted by a probe i_p is obtained by integrating the current density over the effective area for photoemission. Note that this area is generally smaller than that of the entire surface of the body; the ratio of the two areas is equal to one for a planar surface under normal light incidence, but it is of the order of 4 for a spherical body. The photocurrent characteristic is schematically represented in Figure 12; the reference for the voltage is space potential. For negative values of the potential the current is constant and equal to the
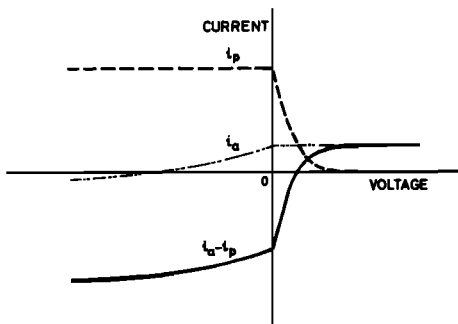

Fig. 12. Current voltage characteristics of a planar probe.

photoelectron saturation current; for positive values of the potential the photocurrent decreases as shown in Figure 11(c, d), for example. In the absence of ambient plasma, no photoelectron may escape, and the floating potential is such that even the most energetic photoelectron must return to the surface.

Considering now the effect of an ambient plasma and neglecting for the moment photoemission, one can see that the current voltage characteristic is that of a Langmuir probe. In the case of a planar probe, the current i_a is practically equal to the plasma electron saturation current for positive values of the probe potential; the ion saturation current, on the contrary, is reached for very negative values of the voltage. The probe is generally floating at a negative voltage that depends on the plasma temperature, unless secondary emission plays a significant role, as was discussed by *Knott* [1972].

Subtracting the photocurrent from the ambient plasma current, we obtain the net current flowing through the probe. In equilibrium the current away from the body must equal the current into it; in a tenuous plasma a small flux of ambient electrons allows an equal flux of the most energetic photoelectrons to escape, and the probe is floating at a positive potential.

It is seen in Figure 12 that Langmuir probe measurements made in interplanetary space must be interpreted with extreme care, since the plasma current may be completely masked by photoemission. In addition, if the photoelectron sheaths of the probe and that of the body with respect to which the probe is biased are overlapping, the existence of a stray photoelectron current through the sheaths will further complicate the task of the experimenter.

When secondary emission is neglected, the floating potential of a body ϕ_F is defined by the equality between photocurrent and plasma current. Assuming that photoelectrons have a Maxwellian energy distribution and that their most probable energy is equal to $e\phi_0$, we can write

$$i_a \simeq I_s \exp - (\phi_F/\phi_0) \qquad (21)$$

Provided that the mean kinetic energy of the photoelectrons is much lower than that of the ambient particles, (21) can be solved for small

values of the probe floating potential ($\phi_r \simeq \phi_0$), assuming that i_a is constant.

We use the average values for photoelectron flux and most probable energy given in Table 2 to estimate the floating potential of a spacecraft at synchronous orbit. Typical values for the ambient electron flux at the geostationary altitude, which can be deducted from the ATS 5 satellite measurements presented by *DeForest and McIlwain* [1971], are of the order of 5 × 10^{12} el/sec m². Reporting these numerical values into (21) yields a typical positive floating potential of the order of 3 volts for a planar surface and 2 volts for a spherical body.

Considering the magnitude of I_s given in Table 2 for various materials, it is seen that the floating potential will be positive under average conditions at the geostationary orbit, even for graphite, which has nevertheless an exceptionally low photoelectron yield. It is possible, however, that the floating potential be negative, even in sunlight, whenever the flux of ambient electrons is larger than that of the photoelectrons. This phenomenon has been observed on the ATS 5 satellite and has been reported by *DeForest* [1972].

The probe conductance at very low frequency is given by the slope of the current voltage characteristic. Around the floating potential the photoelectron current is much more sensitive than the ambient plasma current to variations of the surface potential, and the probe conductance can therefore be computed by using (9) and (13).

CONCLUSION

The energy distribution of photoelectrons emitted by a surface irradiated by sunlight at the earth's orbit was derived by combining laboratory measurements on photoemission and solar flux data. It has been shown that, although the photoyield is a function of the nature of the material, the shape of the energy distribution is very similar for all materials and can be approximated by a Maxwellian model.

The voltage current characteristic and the conductance of planar probes have been computed. The conductance, which should be 0, in the absence of photoemission, can reach typical values of 10–20 μmhos/m².

Various sheath parameters have also been estimated, and it is seen that beyond the plasmapause the electron volume density is larger in the vicinity of a probe than in the ambient plasma.

The exact configuration of the photoelectron sheath in deep space can now be derived for bodies of various shapes by using the results of the present study as input data for already existing simulation programs [*Soop*, 1972].

APPENDIX 1

Perpendicular Velocity Distribution and Associated Energy Distribution

Let $F(v)$ be the normalized perpendicular velocity distribution function corresponding to particles leaving the surface ($v > 0$), and let $N_0/2$ be the density of these particles in the vicinity of the surface. The elementary flux of particles with perpendicular velocities between v and $v + \Delta v$ is

$$\Delta I = \tfrac{1}{2} N_0 v F(v) \ \Delta v \qquad (A1)$$

If the normalized energy distribution function associated with $F(v)$ is $P(\phi)$, where

$$e\phi = \tfrac{1}{2} m v^2 \qquad (A2)$$

and if the total outward flux is I_s, the flux of particles with energies between $e\phi$ and $e(\phi + \Delta\phi)$ is

$$\Delta I = I_s P(\phi) \ \Delta\phi \qquad (A3)$$

Differentiating (A2) and replacing into (A1), we obtain

$$\Delta I = \tfrac{1}{2}(e/m) N_0 F(v) \ \Delta\phi \qquad (A4)$$

Comparing (A3) and (A4) gives

$$P(\phi) = \tfrac{1}{2}(e/m)(N_0/I_s) F(v) \qquad (A5)$$

Characteristic parameters of the distributions are given in Table 1.

Speed Distribution and Energy Distribution

We now take the case of an infinitely small surface emitting particles radially with an isotropic velocity distribution. The outward angular flux is

$$\Delta j = \Delta j_0 \cos \alpha \qquad (A6)$$

where $0 < \alpha < \pi/2$ (see Figure 13), and the total flux is given by

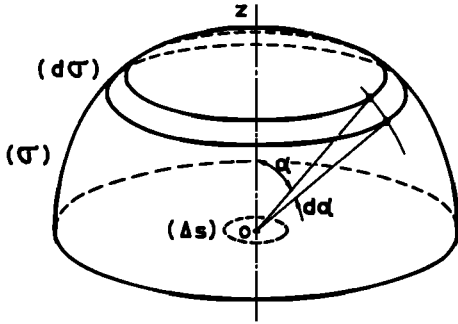$$\Delta J = \int_{(\sigma)} \Delta j \ d\sigma \qquad (A7)$$

Fig. 13. Photoemission from a small sample.

where

$$d\sigma = 2\pi \sin \alpha \, d\alpha \qquad (A8)$$

is the area of the annular ring $(d\sigma)$, shown in Figure 13. Replacing (A6) and (A8) into (A7) and integrating over the hemisphere (σ) of radius unity gives

$$\Delta J = \pi \, \Delta j_0 \qquad (A9)$$

This flux refers only to particles leaving the elementary surface, but there is indeed an equal flux of particles returning to it.

For particles with speeds between u and $u + \Delta u$, the angular flux in the direction $\alpha = 0$ is

$$\Delta j_0 = \tfrac{1}{4}\pi N_0 (4\pi u^2) f(u) u \, \Delta u \qquad (A10)$$

where $f(u)$ is the normalized speed distribution of the particles. Replacing (A10) into (A9) we obtain for the corresponding omnidirectional flux

$$\Delta J = \pi N_0 u^3 f(u) \, \Delta u \qquad (A11)$$

On the other hand, if the energy distribution of the particles leaving the source is $p(\psi)$, where

$$e\psi = \tfrac{1}{2}mu^2 \qquad (A12)$$

and if the total outward flux is I_s, the elementary flux of particles with energies between $e\psi$ and $e(\psi + \Delta\psi)$ is

$$\Delta J = I_s p(\psi) \, \Delta\psi \qquad (A13)$$

Replacing (A12) into (A11), we write

$$\Delta J = 2\pi (e/m)^2 N_0 \psi f(u) \, \Delta\psi \qquad (A14)$$

Equating (A13) and (A14), we obtain

$$p(\psi) = 2\pi (e/m)^2 (N_0/I_s) \psi f(u) \qquad (A15)$$

Various parameters related to the speed and energy distributions are listed in Table 1.

Derivation of the Volume Density and of the Energy Distribution Associated with the Perpendicular Motion of the Particles

Monoenergetic emission. Let us suppose that the energy distribution $p(\psi)$ defined by (A15) has been obtained from the experimental study of a small sample of a given material. With the assumption that the angular dependence of the directional flux is given by (A6), our purpose is to determine the perpendicular velocity distribution, or its associated energy distribution $P(\phi)$ defined by (A5), in the vicinity of a planar surface made of the same material.

With reference to Figure 14, let us first define in a plane (s) a laminar ring (Δs) of area

$$\Delta s = 2\pi r \Delta r \qquad (A16)$$

let us also consider an elementary surface $(\Delta\sigma)$ of area $\Delta\sigma$, perpendicular to oz and at a distance L, arbitrarily small, from (s).

The flux of particles emitted out of (Δs) toward $(\Delta\sigma)$ with a directional flux Δj is given by

$$\Delta i = \Delta j \Delta s \Delta\Omega_\sigma / \Delta\sigma \qquad (A17)$$

where

$$\Delta\Omega_\sigma = \Delta\sigma \cos\alpha / (L^2 + r^2) \qquad (A18)$$

Replacing (A6), (A16), and (A18) into (A17), we obtain

$$\Delta i = \Delta j_0 2\pi r \Delta r \cos^2\alpha / (L^2 + r^2) \qquad (A19)$$
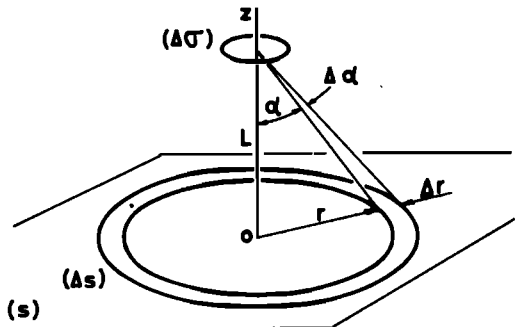

Fig. 14. Photoemission from a planar surface.

which can also be written for monokinetic particles:

$$\Delta i = \tfrac{1}{2} v \Delta n \qquad \text{(A20)}$$

where $\Delta n/2$ is the volume density of particles leaving the surface with perpendicular velocities between v and $v + \Delta v$; it is understood that the density of particles returning to the surface is also $\Delta n/2$.

The perpendicular velocity is given by

$$v = u \cos \alpha \qquad \text{(A21)}$$

which yields after differentiation

$$\Delta v = vr\Delta r/(L^2 + r^2) \qquad \text{(A22)}$$

Replacing (A9), (A21), and (A22) into (A19), we obtain

$$\Delta i = 2\Delta J v \Delta v/u^2 \qquad \text{(A23)}$$

Equating (A20) and (A23) gives

$$\Delta n = 4\Delta J \Delta v/u^2 \qquad \text{(A24)}$$

Integrating with respect to v between o and u, we have the total density of the particles in the vicinity of the surface:

$$n = 4\Delta J/u \qquad \text{(A25)}$$

With equations A2 and A12, equations A23 and A25 become

$$\Delta i = \Delta J \Delta \phi/\psi \qquad \text{(A26)}$$

and

$$n = \Delta J(8m/e\psi)^{1/2} \qquad \text{(A27)}$$

respectively.

Continuous energy distribution. We extend the results given by (A26) and (A27) to the case of a continuous distribution.

Replacing (A13) into (A26) and integrating over the energy distribution, we find

$$\Delta I = I_s \Delta \phi \int_\phi^\infty \frac{p(\psi)}{\psi} d\psi \qquad \text{(A28)}$$

Comparing (A28) with (A3), we obtain

$$P(\phi) = \int_\phi^\infty \frac{p(\psi)}{\psi} d\psi \qquad \text{(A29)}$$

Replacing (A13) into (A27) and integrating over the entire energy distribution, we find for the total electron density in the vicinity of the surface:

$$N_0 = \left(8 \frac{m}{e}\right)^{1/2} I_s \int_0^\infty \frac{p(\psi)}{\sqrt{\psi}} d\psi \qquad \text{(A30)}$$

APPENDIX 2

The following nomenclature is used in this paper:

e electron charge.

E_0 surface electric field on a planar electrode.

f photoelectron speed distribution.

f_w photoelectron energy distribution for a given photon energy.

F distribution function of the velocity component perpendicular to the surface.

g per unit area conductance for a small probe.

g_0 maximum per unit area conductance for a small probe.

G per unit area conductance for a planar probe.

G_0 maximum per unit area conductance for a planar probe.

H photoelectron differential flux.

i_a ambient plasma current collected by a probe.

i_p photoelectron current emitted by a probe.

I photoelectron flux leaving a planar probe.

I_s photoelectron saturation flux.

J photoelectron flux leaving a point source.

m electron mass.

N_0 electron density near the surface.

p normalized photoelectron energy distribution.

P energy distribution associated with the motion perpendicular to a planar surface.

S solar photon energy spectrum.

u photoelectron speed.

u_e photoelectron rms speed.

u_0 speed associated with a monokinetic distribution.

v photoelectron velocity component normal to the surface.

v_e rms value of the velocity component normal to the surface.

v_0 thermal velocity associated with a Maxwellian distribution.

w photon energy.

w_f work function.

Y photoelectric yield per incoming photon.

α angle between the photoelectron velocity vector and the normal to the surface.

δ Dirac impulse symbol.

ϵ_0 vacuum dielectric constant.

λ_0 shielding distance.

Π rectangular function symbol.

σ_0 surface charge density carried by a planar probe.

ϕ' potential of a planar probe.

ϕ_F floating potential of a probe.

ψ' potential of a small probe.

$e\phi$ energy associated with the motion normal to the surface.

$e\phi_a$ average energy associated with the motion normal to the surface.

$e\phi_e$ energy associated with the rms velocity component perpendicular to the surface.

$e\phi_0$ most probable energy associated with a Maxwellian distribution.

$e\psi$ photoelectron energy.

$e\psi_e$ mean kinetic energy.

$e\psi_0$ energy associated with a monokinetic distribution.

$e\psi_p$ most probable energy.

REFERENCES

Allen, C. W., *Astrophysical Quantities,* p. 171, Athlone, London, 1955.

DeForest, S. E., Spacecraft charging at synchronous orbit, *J. Geophys Res., 77,* 651, 1972.

DeForest, S. E., and C. E. McIlwain, Plasma clouds in the magnetosphere, *J. Geophys. Res., 76,* 3587, 1971.

Feuerbacher, B., and B. Fitton, Experimental investigation of photoemission from satellite surface materials, *J. Appl. Phys., 43,* 1563, 1972.

Feuerbacher, B., M. Anderegg, B. Fitton, L. D. Laude, R. F. Willis, and R. J. L. Grard, Photoemission from lunar surface fines and the lunar photoelectron sheath, *Geochim. Cosmochim. Acta, Suppl. 3,* 2655, 1972.

Friedman, H., Rocket spectroscopy, in *Space Science,* edited by D. P. Le Gallet, p. 549, John Wiley, New York, 1963.

Grard, R. J. L., Dynamic behaviour of the photoelectron sheath, 1, *ESRO SN-112 (ESTEC),* Europ. Space Res. and Tech. Centre, Noordwijk, The Netherlands, 1970.

Grard, R. J. L., and J. K. E. Tunaley, Photoelectron sheath near a planar probe in interplanetary space, *J. Geophys. Res., 76,* 2498, 1971.

Hinteregger, H. E., L. A. Hall, and G. Schmidtke, Solar XUV radiation and neutral particle distribution in July 1963 thermosphere, *Space Res., 5,* 1175, 1965.

Knott, K., The equilibrium potential of a magnetospheric satellite in an eclipse situation, *Planet. Space Sci., 20,* 1137, 1972.

Lukirskii, A. P., M. A. Rumsh, and L. A. Smirnov, Monochromator for very soft X-rays which can count the absolute number of quanta, *Opt. Spectros., 9,* 262, 1960.

Soop, M., Report on photosheath calculations for the satellite Geos, *Planet. Space Sci., 20,* 859, 1972.

Trendelenburg, E. A., B. Fitton, D. E. Page, and A. Pedersen, *ELDO/ESRO Sci. Tech. Rev., 2,* 1, 1970.

Walbridge, E., The lunar photoelectron layer, *Intern. Rep.,* High Alt. Observ., Nat. Center for Atmos. Res., Boulder, Colorado, 1971.

Whipple, E. C., Jr., The equilibrium electric potential of a body in the upper atmosphere and in interplanetary space, *NASA Rep. X-615-65-296,* 1965.